Energy-Tailorable Spin-Selective Multifunctional Metasurfaces with Full Fourier Components

Wenwei Liu, Zhancheng Li, Zhi Li, Hua Cheng, Chengchun Tang, Junjie Li, Shuqi Chen,* and Jianguo Tian

Compact integrated multifunctional metasurface that can deal with concurrent tasks represent one of the most profound research fields in modern optics. Such integration is expected to have a striking impact on minimized optical systems in applications such as optical communication and computation. However, arbitrary multifunctional spin-selective design with precise energy configuration in each channel is still a challenge, and suffers from intrinsic noise and complex designs. Here, a design principle is proposed to realize energy tailorable multifunctional metasurfaces, in which the functionalities can be arbitrarily designed if the channels have no or weak interference in *k*-space. A design strategy is demostrated here with high-efficiency dielectric nanopillars that can modulate full Fourier components of the optical field. The spin-selective behavior of the dielectric metasurfaces is also investigated, which originates from the group effect introduced by numerous nanopillar arrays. This approach provides straightforward rules to control the functionality channels in the integrated metasurfaces, and paves the way for efficient concurrent optical communication.

As there has been rapid development of modern fabrication techniques, integrated planar electromagnetic (EM) functional systems have been considered as one of the most challenging research fields in theory and technology. In the past decades, planar integrated manipulation of EM waves has been investigated at different wavebands, such as microwave,[1] terahertz,[2,3] and infrared[4] regions. Artificial metasurfaces composed of customized planar nanostructures have been a research hot spot to manipulate EM waves, which provide a wide platform for deep light–matter interactions at the subwavelength scale.[5–10] Taking advantage of the abundant resonances generated from nanostructures composed of different materials, such as metallic,[11] dielectric,[12,13] and 2D materials,[14] various kinds of metasurfaces have been proposed in the applications of electromagnetically induced transparency,[15] zero-index responses,[16,17] asymmetric spin-orbit interaction,[18,19] structural colors,[20–23] surface waves,[24] topological photonics,[25,26] and so on. Metasurfaces are also a sophisticated and versatile tool to control optical amplitude,[27] phase,[28] polarization,[29] and the combination of these optical dimensions.[30–33] Compared with single-layer metasurfaces, few-layer metasurfaces with two or more overlapping structure layers significantly increase the effective light–matter interaction distances and exploit the integrated functionalities of metasurfaces.[34–39] However, to date the integration of arbitrary optical functionalities onto one single metasurface is still challenging due to the limitation of theoretical design and the absence of full control for multidimensional optical fields.

Recently, integrated multifunctional metasurfaces that can deal with concurrent tasks have drawn much attention of the scientific community.[40–43] One of the designs to realize multifunctional metasurfaces is to divide the device into several areas, and each area serves as one functionality.[44,45] Such designs usually suffer from low information capacity and strong noises originated from channels mixing.[46] Another design utilizes harmonic analysis to distribute all the functionality channels to each nanostructures, which has been widely investigated to achieve polarization-controllable multichannel vortex beams generation.[47–49] Jiang et al. proposed a broadband multipole vortex beams generation for centimeter waves, and opened up the possibilities for multichannel informational gigahertz modulation.[50] However, the abovementioned designs employ intensity- or phase-only manipulation to control the optical fields, which suffer from unavoidable noises for multifunctional optical devices. Especially for the phase-only design,[51] one usually needs to perform complex optimizations

Dr. W. Liu, Dr. Z. Li, Dr. Z. Li, Prof. H. Cheng, Prof. S. Chen, Prof. J. Tian
The Key Laboratory of Weak Light Nonlinear Photonics
Ministry of Education
School of Physics
TEDA Institute of Applied Physics, and Renewable Energy Conversion and Storage Center
Nankai University
Tianjin 300071, China
E-mail: schen@nankai.edu.cn
Prof. H. Cheng, Prof. S. Chen, Prof. J. Tian
The Collaborative Innovation Center of Extreme Optics
Shanxi University
Taiyuan, Shanxi 030006, China
Dr. C. Tang, Prof. J. Li
Beijing National Laboratory for Condensed Matter Physics
Institute of Physics
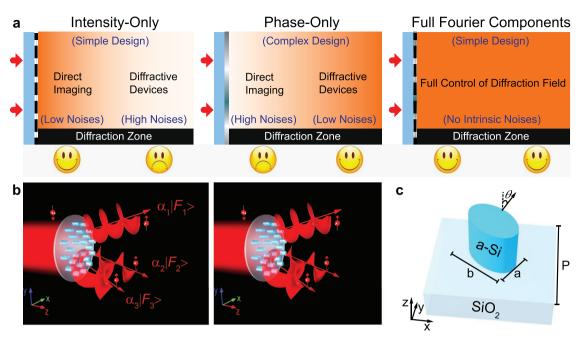Chinese Academy of Sciences
Beijing 100190, China

Figure 1. Realization of the energy tailorable spin-selective multifunctional metasurface. a) Comparison between different methods to manipulate the optical fields in the diffraction zone. With full Fourier components manipulation, the diffraction filed can be fully controlled with simple design, and with no noises in theory, while with intensity- or phase-only design, the applications are limited with intrinsic noises. Direct imaging means imaging directly using the transmission function without diffraction, such as a calibration test target. b) Schematic illustration of spin correlated three-channel vortex beams generated from the full-Fourier-component metasurface, in which the jth functionality $|F_j>$ for σ incidence is designed with energy of α_j. The blocked channel for $-\sigma$ incidence carries no information. c) The unit cell of the metasurface consists of an amorphous silicon elliptic nanopillar with height of 860 nm on the fused silica substrate. The short axis a and the orientation angle θ (define as the crossing angle with y-axis) vary with the required transmission and phase, and the long axis b of the ellipse is set as 465 nm.

and iteration operations to maximize the efficiency, which is time-consuming and the efficiency is theoretically limited due to the existence of unavoidable noises. As demonstrated by Romero and Dickey, the phase-only device either has a single nonzero Fourier component, or has an infinite number of nonzero Fourier components.[52] If we want to design a device with finite Fourier components with the phase-only method, such as a grating, this theorem means that the noises will always exist except for light deflection (a grating with only one diffraction order). Although researchers have exploited simultaneous control of amplitude and phase in recent years,[30] the efficiency is limited and it has not been generally applied in information photonics. In addition, most of the geometric phase–based multifunctional metasurfaces are conjugate for left-handed circularly polarized (LCP) and right-handed circularly polarized (RCP) incidences, leading to a shared information bits of the multifunctional metasurfaces. Here, we analyze the diffraction fields of the metasurfaces in k-space, and propose a theoretical design using full Fourier components to realize energy tailorable multifunctional metasurfaces. The functionalities are not only limited to vortex beams. Taking vortex beams, calibration test targets, plane waves, and focusing as examples, we propose a judicious design of dielectric nanopillars and demonstrate the validity of the proposed theory. Furthermore, the spin-selective characteristic generated from a group effect is also demonstrated, which breaks the conjugate symmetry of the geometric phase for LCP and RCP incidences. The proposed blocked channel for $-\sigma$ incidence may find applications in optical encryption and disguised imaging.

The schematic of the designed spin-selective multifunctional metasurface is shown in **Figure 1**. For the traditional intensity-only designs, the diffractive devices suffer from high noises because the diffraction field is the superposition of two conjugated fields.[66] For example, an amplitude grating always has symmetric diffraction orders. Thus, researchers prefer phase-only designs to manipulate the diffraction fields, which also suffer from unavoidable noises due to the lack of full Fourier components.[52] In addition, the phase-only devices take optimization or iteration operations to maximize the efficiency, leading to time-consuming and complex designs. In contrast, our designs employ full Fourier components (intensity and phase) to manipulate the optical fields, which could significantly boost the applications based on the proposed platform without noises in theory. The designed metasurface can convert the incident σ light to $-\sigma$ light of different functionalities with predefined energy ratios, and the functionalities are not only limited to vortex beams. Although independent control of amplitude and phase is a basic condition to realize energy tailorable multifunction, we cannot design the metasurface by directly varying the amplitude of each channel because the energy of each channel is also associated with its phase distribution. For example, the deep sub-wavelength metasurface with identical phase delay in each unit cell can generate a plane wave front. However, the deep subwavelength metasurface with 0 and π phase delay in every other unit cell cannot scatter the incident wave to the far-field region since the phase gradient is much larger than the wave vector in free space, leading to evanescent waves near the metasurface. As an example, we calculated the diffraction field

distribution for three different phase profiles, and the calculated total energy of the corresponding diffraction field varies from 1.33×10^{-5} to 2.48×10^{-6} for the designed three phase profiles (in arbitrary unit, see Figure S1 in the Supporting Information). To take phase distribution of each functionality of the metasurface into consideration, a momentum analysis method[53] was adopted to calculate the far-field diffraction in k-space (defined as the functionality function)

$$\mathcal{F}(\mathbf{k}) = \sum_i \frac{|t_i|}{\pi} e^{-i(\phi_i + \mathbf{k} \cdot \mathbf{r}_i)} \prod_{\nu=x,y} \frac{\sin(k_\nu T_{\nu i}^{MS}/2)}{k_\nu} \tag{1}$$

where t_i, ϕ_i, $\mathbf{r}_i$, and $T_{\nu i}^{MS}$ indicate the electric transmission/reflection, phase delay, spatial location, and equivalent size of each unit cell, respectively. For an arbitrary M-function metasurface, the total functionality function is the sum of each one

$$\mathcal{F} = \sum_{j=1}^{M} \mathcal{F}_j \tag{2}$$

The ith unit cell should be designed according to the formula $A_i e^{-i\phi_i} = \sum_{j=1}^{M} \sqrt{c_j} A_{ji} e^{-i\phi_{ji}}$, where $A_{ji} = \frac{|t_{ji}|}{\pi} \prod_{\nu=x,y} \frac{\sin(k_\nu T_{\nu ji}^{MS}/2)}{k_\nu}$ is the effective amplitude of the jth functionality and the ith unit cell, c_j is a constant associated with the energy ratio of the jth functionality. To ensure that the effective amplitude is no more than one, we need to normalize and replace A_i with $A_i' = \frac{A_i}{Max\{A_i\}|_{1 \le i \le N}}$. The total energy of the diffraction field is $E = \int_{-k_0}^{k_0} |\mathcal{F}(k)|^2 \, dk$. Thus, the total energy can be written as

$$E = \sum_{j=1}^{M} c_j E_j + \sum_{m \neq n} \sqrt{c_m c_n} \int_{-k_0}^{k_0} \mathcal{F}_m(k) \mathcal{F}_n^*(k) \, dk \tag{3}$$

where $E_j = \int_{-k_0}^{k_0} |\mathcal{F}_j(k)|^2 \, dk$ is the total energy of the jth functionality. For simplicity, we assume the functionality channels do not interact with each other in k-space, which can be mathematically expressed with $\mathcal{F}_n(k)|_{\partial k_m} = 0$. Thus, Equation (3) can be simplified according to $\int_{-k_0}^{k_0} \mathcal{F}_m(k) \mathcal{F}_n^*(k) \, dk = \int_{\partial k_m} \mathcal{F}_m(k) \mathcal{F}_n^*(k) \, dk + \int_{\partial k_n} \mathcal{F}_m(k) \mathcal{F}_n^*(k) \, dk = 0$, where $m \neq n$. The total energy of $\mathcal{F}$ is
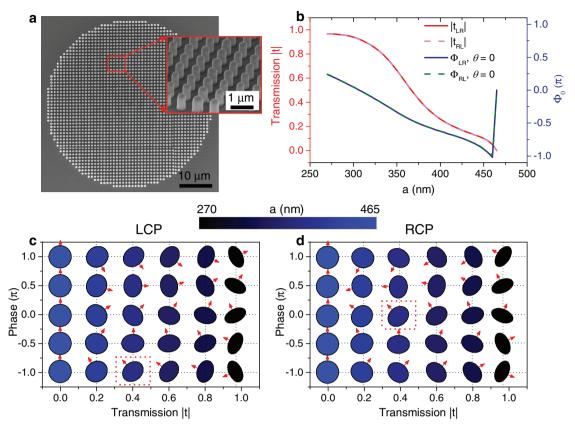
$$E = \sum_{i=1}^{M} c_j E_j \tag{4}$$

Thus, by employing full Fourier components A_i' and ϕ_i, the control of energy ratio of $\mathcal{F}_j$ could be realized. The energy ratio is defined as $\alpha_j = c_j E_j / E$. Since the full Fourier components could completely describe the diffraction fields of the devices, we do not need to further optimize to maximize the efficiency.

The proposed metasurfaces are designed with amorphous silicon nanopillars for the operation wavelength of 1550 nm. Such large aspect-ratio dielectric structures with high refraction index can generate waveguide modes[54,55] and support Fabry–Pérot resonances,[56,57] leading to deep modulation of optical amplitude,[58] phase,[59,60] and polarization.[61] We optimized the silicon nanopillars with height of 860 nm for

different diameters and orientations to realize the required optical modulation (Figure 1c). The simulated nanopillar with short axis of 270 nm and long axis of 465 nm serves as an efficient half-wave plate with transmission of 0.97, which can convert the incident polarization to its orthogonal state (see Figure S2 in the Supporting Information). The fabricated metasurface is shown in **Figure 2**a. With the increasing of the short axis, the transmission of the cross-polarized light gradually decreases to zero until the length of short axis equals to that of the long axis (Figure 2b). This is because the nanopillar becomes symmetric in x–y plane when the ellipse turns to be a circle, unable to realize polarization conversion anymore. The nanopillars possess propagation phase and geometric phase simultaneously.[33,62] For LCP/RCP incidence, the simulated propagation phase delay of the nanopillars varies over 1.25π for different lengths of short axis (with the orientation angle $\theta = 0$). In Figure 2c,d we depicted the geometries and orientations of the nanopillars for any predefined phase and transmission with LCP/RCP incidence. The phase can be written as $\phi = \Phi_0 + 2\sigma\theta$, where Φ_0 is the propagation phase and $\sigma = \pm 1$ is the helicity of the incident light. For a given ϕ, the orientation angle is $\theta = (\phi - \Phi_0)/2\sigma$, which varies with Φ_0 and σ. As a result, although the propagation phase for LCP/RCP incidence is the same and shows no chirality, the orientation angles of the nanopillars differ from each other for LCP/RCP incidence, which induces spin-selective functionalities and chirality of the metasurfaces. This intriguing property introduced by group effects of the nanopillar arrays will be discussed in detail in the following parts. The waveguide modes in large aspect-ratio dielectric nanopillars usually lead to broadband responses. We simulated the transmission and phase delay of the nanopillars for different lengths of short axis over 1200 to 1800 nm, where the orientation angle θ is fixed as 0 (**Figure 3**a,b). The simulated results show a broadband high-transmission area accompanied with three resonant lines cutting the spectra. The linewidths of such resonances are generally very narrow due to the rigid condition to realize Fano resonances.[63–66] The high-transmission areas dominate most of the transmission spectra. The simulated phase is more smooth and covers $[0, 2\pi)$ for the selected waveband. Four resonant waveguide modes marked in Figure 3a are also shown in Figure 3c, which shows near field magnetic distributions of the nanopillars. The light energy is mainly confined inside the nanopillar and has negligible dependence on the neighboring nanopillars, which is a basic condition to locally control the scattered EM field.[53,54] With the decreasing of the wavelength, the number of wave loops will increase due to the decreasing of effective wavelength λ/n_{eff}, where n_{eff} is the effective refractive index of the dielectric waveguide and can be computed through a step-index circular waveguide model. Such results show that although the designed metasurfaces are not broadband, the proposed design could be easily changed to other waveband by adjusting the length of the axis.

We employed the proposed theory and simulated nanopillars to realize the energy tailorable multifunctional metasurfaces. The electron-beam lithography was adopted to fabricate the metasurfaces with squared subwavelength lattice. The radii of the fabricated metasurfaces are 50 μm. A custom-built setup is used to measure different functionality channels in k-space
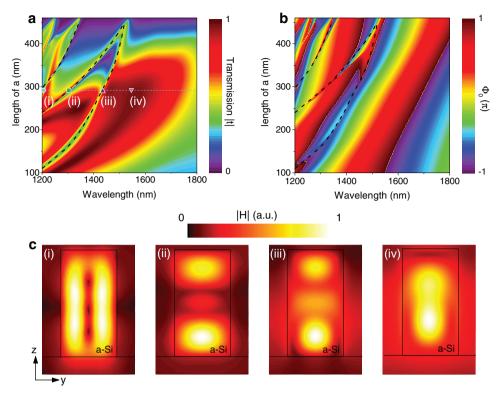
Figure 2. Design of the dielectric nanopillars. a) Scanning electron microscopy (SEM) images of the fabricated metasurface. b) Simulated cross-polarization transmission for different lengths of a and corresponding initial phase Φ_0 with $\theta = 0$. The incident wavelength is 1550 nm. c,d) The dimensions and orientations of the nanopillars for LCP (c) and RCP (d) incidences, with a given transmission and phase. The dashed red boxes indicate the structures with close orientations but large phase difference of π for LCP and RCP incidences.

(**Figure 4**a). As an example, we designed four samples with three channels in each one. The three channels were a three-order vortex beam (F_1), a one-order vortex beam (F_2), and a plane wave (F_3), respectively. The transmitted RCP waves were detected for LCP incidence. We obtained the numerical intensity matrix of the light field in k-space using the LABVIEW-based InGaAs camera, and integrated the matrix within each functionality area to quantify its energy. We also theoretically calculated the energy following the formula $E_j = \int_{-k_0}^{k_0} |\mathcal{F}_j(k)|^2 \, dk$.

As shown in Figure 4b, the calculated and measured energy ratios are close to the designed ones, demonstrating the validity of the proposed theory. The theoretically calculated energy distributions for the four samples are shown in Figure 4c–f. Compared with the theoretical calculation, the measured energy distributions also show the evident energy variation in each channel but with zero-order light in the center, which is also the original point of k-space (Figure 4g–j). The zero-order light is attributed to imperfections of fabrication and measurement, and could be easily blocked by a Fourier filter in real applications. It is worth mentioning that the larger the metasurface is, the sharper the functionality channel in k-space will be.[67,68] The radius of the fabricated samples is 50 µm, which generates sharp energy distribution, and can just be identified by the InGaAs camera in the measurement. The measured noises in the energy distributions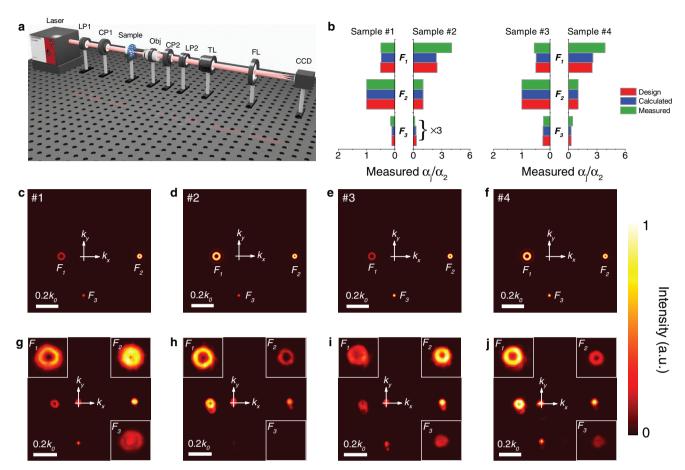 have tolerable impact on the Pearson correlation coefficients between theory and experiments (see Figure S3 in the Supporting Information). To increase the visibility of the channels, we also captured the light distribution from a small defocusing plane (2 mm from the focal plane), as shown in the insets of Figure 4g–j. The defocusing distance is much smaller than the focal length of the Fourier lens, which guarantees that each functionality channel still does not interact with each other. On the other hand, we know that a focused vortex beam is still a vortex beam with donut-shaped light distribution, no matter whether we observe the light distribution at the focal plane or not. The difference is that the diameter of the donut-shaped ring at the focal plane is much smaller than those at the other planes. Therefore, the employed defocusing measurement is reliable to make the donut-shaped light distribution more clearly. The other measurements, such as the intensity of each channel, were still performed at the focal plane. We also simulated the field distribution for a designed metasurface with radius of 16 µm (see Figure S4 in the Supporting Information). We extracted the field distribution at a cut plane with 5 µm from top of the nanopillars, and performed fast Fourier transform (FFT) with MATLAB to get the simulated field in k-space, which is in good agreement with the theory and experiments. The theoretical efficiency of the design is about 40%, which is lower than phase-only multifunctional metasurfaces. The proposed design provides an alternative method to those applications in which low noises is more pivotal.

**ADVANCED
SCIENCE NEWS**

www.advancedsciencenews.com

**ADVANCED
MATERIALS**

www.advmat.de

Figure 3. The resonance behavior of the nanopillars to realize the energy tailorable spin-selective metasurfaces. a,b) Simulated transmission (a) and phase delay (b) (normalized with π) at a broad wavelength range with different lengths of short axis of the nanopillars. The black dashed lines indicate sharp Fano resonances, which lead to an abrupt change in the transmission spectra. c) Magnetic intensity distribution at four positions marked in (a) with $a = 292$ nm, which shows different waveguide modes of the nanopillars.

As discussed above, the designed metasurfaces possess spin-selective and chiral behaviors considering their group functionalities. Although the cross-polarized transmission and propagation phase remain the same for LCP and RCP incidences, the nanopillars play different roles in the metasurfaces for different incident polarizations. For example, for LCP incidence, we randomly selected three nanopillars with $|t_{LR1}| = 0.97$, $\phi_{LR1} = \pi$; $|t_{LR2}| = 0.62$, $\phi_{LR2} = \pi/2$; $|t_{LR3}| = 0.15$, $\phi_{LR3} = 0$, the corresponding transmission and phase delay for RCP incidence will be $|t_{RL1}| = 0.97$, $\phi_{RL1} = -0.52\pi$; $|t_{RL2}| = 0.62$, $\phi_{RL2} = -1.24\pi$; $|t_{RL3}| = 0.15$, $\phi_{RL3} = -1.52\pi$, whose phase distributions are random compared with those of the LCP incidence. That means if we design the phase distribution of the multifunctional metasurface with predefined LCP incidence, the metasurface will lose the information of the wave front for RCP incidence, and vice versa. As shown in **Figure 5**a, we measured the energy distribution for RCP incidence at the focal plane, and the energy is low and dispersive (blocked channel), demonstrating the spin-selective behavior of the designed metasurfaces. It is worth noting that this spin-selective characteristic originates from the arrangements of massive unit cells, and is one of the group effects. Although the transmission of the nanostructures shows no chirality, the spin-selective behavior is related to the transmission, propagation phase and Pancharatnam–Berry phase, simultaneously. Another application is to achieve the calibration test target. As shown in Figure 5b, we employed high polarization conversion pixels ($a = 270$ nm, $b = 465$ nm) and no-polarization conversion pixels (cylindrical pixels) to realize

high-contrast 1951 USAF resolution test target, with orders of 6 and 7. For LCP-RCP or RCP-LCP conversion, the designed target is a negative one, and for LCP-LCP or RCP-RCP conversion, it is a positive one. Interestingly, compared with the blocked channels in the vortex beams generation, the calibration metasurfaces maintain the same number of channels for different polarization conversion. This is due to the symmetry of the rotation-free dielectric pixels. The calibration design also demonstrates that the proposed platform can combine the intensity- and phase-only applications together.

Our theory is not only limited to vortex beams. Any designs with weak interference between different channels in k-space are also suitable. We designed a two-function metasurface, which can combine metalens and anomalous refraction simultaneously. The schematic of the design is shown in **Figure 6**a. The designed metalens occupies a phase distribution of $\phi_1 = -k_0\left(\sqrt{r^2 + f^2} - f\right)$,[65] with focal length of $f = 40$ µm, and the anomalous refraction has a phase distribution of $\phi_2 = -0.2k_0x$ with refraction angle of 11.5°. The total size of the metasurface is 200 µm. We combined the two functionalities with different energy ratios following the proposed theory, and compared the calculated and designed energy ratios in Figure 6b. It turns out that the two results meet well with each other, demonstrating that the proposed theory can be applied to realize versatile functionalities, with high accuracy and broad design range (from 2^{-4} to 2^4). We also calculated the intensity distribution in k-space for $\alpha_2/\alpha_1 = 1$ (Figure 6c). For the metalens, most of the energy distributes at large k components. For

Figure 4. Demonstration of the energy tailorable multifunction with LCP incidence. a) The incident polarization is controlled by a polarizer (LP1) and a quarter-wave plate (CP1). The output light is collected by an objective (Obj) and a tube lens (TL), and the transmitted polarization is detected by a quarter-wave plate (CP2) and a polarizer (LP2). Then, a Fourier lens (FL) and an InGaAs camera are adopted to measure the far-field diffraction in k-space. b) The designed, calculated and measured energies of each functionality of the four metasurface samples, in which $|F_1\rangle$, $|F_2\rangle$, $|F_3\rangle$ are designed as vortex light with order of 3, 1, 0, respectively. c–f) Theoretical $|E|^2$ distributions of three functionalities in k-space for different designed samples. g–j) Measured light distributions of three functionalities in k-space, which are obtained from measured numerical intensity matrices. The insets in (g–j) show the enlarged images of each functionality in 2 mm defocusing plane captured with an InGaAs camera.

the anomalous refraction, the energy locates at $-0.2k_0$, showing a δ-function-like profile. On the other hand, for the metalens, most of the energy is confined at the focal point. The intensity of the electric field of the metalens is much smaller than that of the anomalous refraction at areas away from the focal point. Thus, the functionalities of the metasurface can also be distinguished in real space (Figure 6c,d).

If existing weak interference in k-space between different channels, the energy tailorable functionality can also be realized to meet the scalar superposition condition in Equation (4). However, this limitation can be further released if we can find a method or a space to separate the overlapping functionalities. The interference factor in Equation (3) can be eliminated via transformation of coordinates in k-space, which also means de-multiplexing in a new space/coordinate. One of the possible methods to realize this strategy may be utilizing multilayer metasurfaces, which have recently been adopted to correct chromatic aberrations of metalenses.[66] The spin-selective behavior, which is attributed to a group effect, occurs when numerous nanopillars gather in one device. It is known that

group effects are mainly associated with symmetries, such as topological photonics and phononics.[26,69] Such intriguing properties may have deep impact on theoretical design of planar integrated devices.

In summary, the energy tailorable spin-selective metasurfaces, which can precisely control the energy configuration with a spin-selective behavior, are demonstrated. We utilized the momentum analysis method to deal with the field distribution of each functionality, and in return to compute the energy configuration of the integrated metasurfaces. The design strategy has been demonstrated by the amorphous silicon nanopillars, which can efficiently manipulate the full Fourier components of optical fields. The measured, calculated, and predefined energy distributions can match with each other in a broad design range. The spin-selective behavior of the multifunctional metasurfaces is resulting from a group effect with numerous nanopillar arrays, although a single nanopillar shows no chirality. The spin-selective calibration test targets were also demonstrated. The proposed design strategy is suitable for any integrated functionalities with weak interference in k-space between different
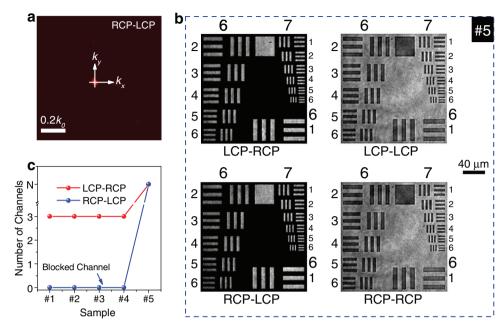
Figure 5. Measured spin-selective behaviors of the metasurfaces. a) Measured LCP light distributions for RCP incidence in the focal plane of Sample #1. b) Measured light distributions for direct imaging of 1951 USAF resolution test target designed with the metasurface (Sample #5). For LCP incidence, the transmitted image of RCP/LCP light is a negative/positive target, respectively. For RCP incidence, similar phenomena can also be observed. c) The number of information channels the light beam carries. For LCP-RCP conversion, the light carries three channels (Sample #1−#4), while for RCP-LCP conversion the information channel is blocked (Sample #1−#4). As a contrast, for Sample #5 the light carries the same information channels for LCP-RCP and RCP-LCP conversion. Note that we do not define the exact value of the number of channels for Sample #5, since the resolution test target is an image.

channels. Our approach does not suffer from intrinsic noises and complex optimization processes, and can find some applications in optical concurrent communication, computation, and imaging diagnostics.

Experimental Section

Sample Fabrication: The dielectric metasurfaces were fabricated on a fused silica substrate. First, a layer of 860 nm amorphous silicon was coated on the substrate with plasma enhanced chemical vapor deposition (PECVD) method at the temperature of 380 °C. Then a layer of PMMA with thickness of 200 nm and a layer of Pedot:PSS with thickness of 35 nm were spin coated on the substrate by sequence. The Pedot:PSS layer was intended for charge release during the electron-beam lithography (EBL) process employing a 100 kV voltage, 200 pA current, and 950 μC cm⁻² dose. To control the lateral size of nanopillars, Beamer, a software from Genysis ltd., was employed to rescale the layout pattern considering the process broadening. As a result, the scale precision of the nanopillars with random angles can be as high as less than 10 nm. After the EBL process, the Pedot:PSS layer was removed with pure water for 60 s and PMMA was developed with MIKE\IPA(1:3) for 40 s. Then a 50 nm Cr layer was deposited on the resist with electron beam evaporation deposition (EBD) method. Then the Cr film was striped by removing PMMA with hot acetone at degree of 60 °C for 20 min, which was followed by HBr plasma dry etching with ICP machine. The residue Cr resist was remove by wet etching method. Finally, a 3 nm Cr layer was coated for scanning electron microscopy (SEM) and then removed with wet etching method before optical measurement.

Simulation and Design: The amorphous silicon elliptic nanopillars were simulated through finite element method (FEM)-based COMSOL Multiphysics to find the resonances of the structure. With σ incidence

($\sigma = \pm 1$ indicates LCP/RCP light), the amplitude and phase of the transmitted $-\sigma$ components were computed by the electric projection $\langle -\sigma | E \rangle$. The permittivity of the amorphous silicon was taken from ref. [70], and the substrate was fused silica with refractive index of 1.5. During the simulation, the incident light was set at the substrate side to guarantee that the transmitted light propagates in free space. After finding a nanopillar serving as a perfect half-wave plate at 1550 nm, the short axis of the ellipse was gradually increased to get a decreasing amplitude modulation. The phase modulation was realized through Pancharatnam–Berry phase and propagation phase. The group effects of the multifunctional metasurfaces were calculated through the momentum analysis method,[53] which can conveniently handle the field distributions in *k*-space. The energy distribution was integrated for each functionality channel of the calculated field in *k*-space, and the calculated energy intensity was obtained in Figure 4b. Also, the field distribution was simulated for a designed metasurface with radius of 16 μm (see Figure S4 in the Supporting Information). The field distribution was extracted at a cut plane with 5 μm from top of the nanopillars, and fast Fourier transform (FFT) was performed with MATLAB to get the simulated field in *k*-space.

Measurement Procedure: The measurement setup consisted of a super-continuous laser (NKT SuperK EXR-20, $\lambda = 1550$ nm) whose polarization was controlled by a linear polarizer and a quarter-wave plate pair to get LCP/RCP incidence. Another quarter-wave plate and linear analyzer pair were utilized to acquire the RCP/LCP output components of the sample. Since only the cross-polarization light was detected, the co-polarization light would not be the noise background of the signal even the size of the incident light beam is much larger than that of the sample. The transmitted signal was collected by an objective (Sigma Near Plan Apo 50×, NA = 0.67) and a tube lens (Thorlabs, TL200-3P). Then, a Fourier lens was adopted to realize Fourier transform of the transmitted signal at its focal plane, which was imaged by an InGaAs camera (HAMAMATSU InGaAs C10633). The measured energy
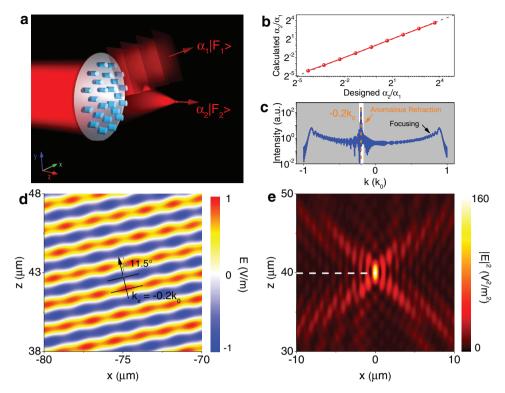
Figure 6. Energy tailorable anomalous refraction and focusing. a) Schematic of the multifunctional metasurface that can simultaneously realize anomalous refraction ($|F_1\rangle$) and focusing ($|F_2\rangle$), with arbitrarily designed energy assignment. b) Calculated energy ratio of α_2/α_1 (red dotted line) as a function of the designed energy ratio. The gray dashed line indicates that the calculated energy ratios equal to the designed ones. c) Calculated logarithmic energy distribution in k-space for $\alpha_2/\alpha_1 = 1$. The designed metasurface with total size of 200 µm possesses a large diffraction peak at $k = -0.2k_0$, which indicates a scattered plane wave propagating along k direction. d) The electric field distribution of the anomalous refraction away from the focusing area. e) The $|E|^2$ distribution near the focal point.

was acquired through the following method. First, the intensity matrix without incident light η was obtained by a LABVIEW-based InGaAs camera. Second, the intensity matrix at the focal plane of the Fourier lens x was captured using the same method. Third, the final intensity matrix calculated with $x-\eta$ was imported to a data analysis software MATLAB to integrate the total energy in each functionality area. Then, we used zero-order light as the origin of the coordinate, and used the distance between zero-order light and F_1 to calibrate the dimensions in k-space.

Supporting Information

Supporting Information is available from the Wiley Online Library or from the author.

Conflict of Interest

The authors declare no conflict of interest.

[1] D. Deslandes, K. Wu, *IEEE Microwave Wireless Compon. Lett.* **2001**, *11*, 68.

[2] M. Nagel, P. Haring Bolivar, M. Brucherseifer, H. Kurz, A. Bosserhoff, R. Büttner, *Appl. Phys. Lett.* **2002**, *80*, 154.

[3] G. Liang, E. Dupont, S. Fathololoumi, Z. R. Wasilewski, D. Ban, H. K. Liang, Y. Zhang, S. F. Yu, L. H. Li, A. G. Davies, E. H. Linfield, H. C. Liu, Q. J. Wang, *Sci. Rep.* **2015**, *4*, 7083.

[4] L. Bi, J. Hu, P. Jiang, D. H. Kim, G. F. Dionne, L. C. Kimerling, C. A. Ross, *Nat. Photonics* **2011**, *5*, 758.

[5] S. Xiao, F. Zhong, H. Liu, S. Zhu, J. Li, *Nat. Commun.* **2015**, *6*, 8360.

[6] N. Yu, P. Genevet, M. A. Kats, F. Aieta, J. P. Tetienne, F. Capasso, Z. Gaburro, *Science* **2011**, *334*, 333.

[7] Z. Liu, Z. Li, Z. Liu, J. Li, H. Cheng, P. Yu, W. Liu, C. Tang, C. Gu, J. Li, S. Chen, J. Tian, *Adv. Funct. Mater.* **2015**, *25*, 5428.

[8] X. Yin, Z. Ye, J. Rho, Y. Wang, X. Zhang, *Science* **2013**, *339*, 1405.

[9] X. Luo, *Sci. China: Phys., Mech. Astron.* **2015**, *58*, 594201.

[10] M. Khorasaninejad, F. Capasso, *Science* **2017**, *358*, eaam8100.

[11] A. Pors, M. G. Nielsen, R. L. Eriksen, S. I. Bozhevolnyi, *Nano Lett.* **2013**, *13*, 829.

[12] K. Fan, J. Zhang, X. Liu, G. F. Zhang, R. D. Averitt, W. J. Padilla, *Adv. Mater.* **2018**, *30*, 1800278.

[13] R. Zuo, W. Liu, H. Cheng, S. Chen, J. Tian, *Adv. Opt. Mater.* **2018**, *6*, 1800795.

[14] H. Cheng, S. Chen, P. Yu, W. Liu, Z. Li, J. Li, B. Xie, J. Tian, *Adv. Opt. Mater.* **2015**, *3*, 1744.

[15] Y. Yang, I. I. Kravchenko, D. P. Briggs, J. Valentine, *Nat. Commun.* **2014**, *5*, 5753.

[16] W. D. Newman, C. L. Cortes, J. Atkinson, S. Pramanik, R. G. Decorby, Z. Jacob, *ACS Photonics* **2015**, *2*, 2.

[17] Y. Li, S. Kita, P. Muñoz, O. Reshef, D. I. Vulis, M. Yin, M. Lončar, E. Mazur, *Nat. Photonics* **2015**, *9*, 738.

[18] F. Zhang, M. Pu, J. Luo, H. Yu, X. Luo, *Opto-Electron. Eng.* **2017**, *44*, 319.

[19] F. Zhang, M. Pu, X. Li, P. Gao, X. Ma, J. Luo, H. Yu, X. Luo, *Adv. Funct. Mater.* **2017**, *27*, 1704295.

[20] J. Proust, F. Bedu, B. Gallas, I. Ozerov, N. Bonod, *ACS Nano* **2016**, *10*, 7761.

[21] Y. Lee, M. K. Park, S. Kim, J. H. Shin, C. Moon, J. Y. Hwang, J. C. Choi, H. Park, H. R. Kim, J. E. Jang, *ACS Photonics* **2017**, *4*, 1954.

[22] C. S. Park, V. R. Shrestha, W. Yue, S. Gao, S. S. Lee, E. S. Kim, D. Y. Choi, *Sci. Rep.* **2017**, *7*, 2556.

[23] B. Yang, W. Liu, Z. Li, H. Cheng, D. Y. Choi, S. Chen, J. Tian, *Nano Lett.* https://doi.org/10.1021/acs.nanolett.8b04923.

[24] Q. Xu, X. Zhang, Y. Xu, C. Ouyang, Z. Tian, J. Gu, J. Li, S. Zhang, J. Han, W. Zhang, *Laser Photonics Rev.* **2017**, *11*, 1600212.

[25] J. S. Gomez-Diaz, M. Tymchenko, A. Alù, *Phys. Rev. Lett.* **2015**, *114*, 233901.

[26] A. B. Khanikaev, G. Shvets, *Nat. Photonics* **2017**, *11*, 763.

[27] Z. Wang, H. Jia, K. Yao, W. Cai, H. Chen, Y. Liu, *ACS Photonics* **2016**, *3*, 2096.

[28] L. Huang, X. Chen, H. Mühlenbernd, G. Li, B. Bai, Q. Tan, G. Jin, T. Zentgraf, S. Zhang, *Nano Lett.* **2012**, *12*, 5750.

[29] T. Lepetit, B. Kanté, *Nat. Photonics* **2015**, *9*, 709.

[30] L. Liu, X. Zhang, M. Kenney, X. Su, N. Xu, C. Ouyang, Y. Shi, J. Han, W. Zhang, S. Zhang, *Adv. Mater.* **2014**, *26*, 5031.

[31] M. Kim, A. M. H. Wong, G. V. Eleftheriades, *Phys. Rev. X* **2014**, *4*, 041042.

[32] A. Arbabi, Y. Horie, M. Bagheri, A. Faraon, *Nat. Nanotechnol.* **2015**, *10*, 937.

[33] J. P. Balthasar Mueller, N. A. Rubin, R. C. Devlin, B. Groever, F. Capasso, *Phys. Rev. Lett.* **2017**, *118*, 113901.

[34] A. Arbabi, E. Arbabi, Y. Horie, S. M. Kamali, A. Faraon, *Nat. Photonics* **2017**, *11*, 415.

[35] H. Cheng, Z. Liu, S. Chen, J. Tian, *Adv. Mater.* **2015**, *27*, 5410.

[36] B. Groever, W. T. Chen, F. Capasso, *Nano Lett.* **2017**, *17*, 4902.

[37] Z. Li, W. Liu, H. Cheng, J. Liu, S. Chen, J. Tian, *Sci. Rep.* **2016**, *6*, 35485.

[38] S. Chen, Z. Li, W. Liu, H. Cheng, J. Tian, *Adv. Mater.* **2019**, *31*, 1802458.

[39] S. Chen, Y. Zhang, Z. Li, H. Cheng, J. Tian, *Adv. Opt. Mater.* **2019**, *7*, 1801477.

[40] T. Cai, S. Tang, G. Wang, H. Xu, S. Sun, Q. He, L. Zhou, *Adv. Opt. Mater.* **2017**, *5*, 1600506.

[41] J. Ding, S. An, B. Zheng, H. Zhang, *Adv. Opt. Mater.* **2017**, *5*, 1700079.

[42] Q. Wang, X. Zhang, E. Plum, Q. Xu, M. Wei, Y. Xu, H. Zhang, Y. Liao, J. Gu, J. Han, W. Zhang, *Adv. Opt. Mater.* **2017**, *5*, 1700277.

[43] J. W. Stewart, G. M. Akselrod, D. R. Smith, M. H. Mikkelsen, *Adv. Mater.* **2017**, *29*, 1602971.

[44] X. Chen, M. Chen, Q. Mehmood Muhammad, D. Wen, F. Yue, C.-W. Qiu, S. Zhang, *Adv. Opt. Mater.* **2015**, *3*, 1201.

[45] D. Lin, A. L. Holsteen, E. Maguid, G. Wetzstein, P. G. Kik, E. Hasman, M. L. Brongersma, *Nano Lett.* **2016**, *16*, 7671.

[46] E. Maguid, I. Yulevich, D. Veksler, V. Kleiner, M. L. Brongersma, E. Hasman, *Science* **2016**, *352*, 1202.

[47] F. Yue, D. Wen, C. Zhang, B. D. Gerardot, W. Wang, S. Zhang, X. Chen, *Adv. Mater.* **2017**, *29*, 1603838.

[48] J. Jin, M. Pu, Y. Wang, X. Li, X. Ma, J. Luo, Z. Zhao, P. Gao, X. Luo, *Adv. Mater. Technol.* **2017**, *2*, 1600201.

[49] Y. Li, X. Li, L. Chen, M. Pu, J. Jin, M. Hong, X. Luo, *Adv. Opt. Mater.* **2017**, *5*, 1600502.

[50] Z. H. Jiang, L. Kang, W. Hong, D. H. Werner, *Phys. Rev. Appl.* **2018**, *9*, 064009.

[51] G. Zheng, H. Mühlenbernd, M. Kenney, G. Li, T. Zentgraf, S. Zhang, *Nat. Nanotechnol.* **2015**, *10*, 308.

[52] L. Romero, F. Dickey, *Prog. Opt.* **2010**, *54*, 319.

[53] W. Liu, Z. Li, H. Cheng, S. Chen, J. Tian, *Phys. Rev. Appl.* **2017**, *8*, 014012.

[54] M. Khorasaninejad, A. Y. Zhu, C. Roques-Carmes, W. T. Chen, J. Oh, I. Mishra, R. C. Devlin, F. Capasso, *Nano Lett.* **2016**, *16*, 7229.

[55] R. C. Devlin, M. Khorasaninejad, W. T. Chen, J. Oh, F. Capasso, *Proc. Natl. Acad. Sci. USA* **2016**, *113*, 10473.

[56] A. Arbabi, Y. Horie, A. J. Ball, M. Bagheri, A. Faraon, *Nat. Commun.* **2015**, *6*, 7069.

[57] S. M. Kamali, A. Arbabi, E. Arbabi, Y. Horie, A. Faraon, *Nat. Commun.* **2016**, *7*, 11618.

[58] B. Yang, W. Liu, Z. Li, H. Cheng, S. Chen, J. Tian, *Adv. Opt. Mater.* **2018**, *6*, 1701009.

[59] M. Khorasaninejad, F. Capasso, *Nano Lett.* **2015**, *15*, 6709.

[60] S. Chen, Z. Li, Y. Zhang, H. Cheng, J. Tian, *Adv. Opt. Mater.* **2018**, *6*, 1800104.

[61] X. Zang, F. Dong, F. Yue, C. Zhang, L. Xu, Z. Song, M. Chen, P. Y. Chen, G. S. Buller, Y. Zhu, S. Zhuang, W. Chu, S. Zhang, X. Chen, *Adv. Mater.* **2018**, *30*, 1707499.

[62] R. C. Devlin, A. Ambrosio, N. A. Rubin, J. P. B. Mueller, F. Capasso, *Science* **2017**, *358*, 896.

[63] Y. Zhang, W. Liu, Z. Li, Z. Li, H. Cheng, S. Chen, J. Tian, *Opt. Lett.* **2018**, *43*, 1842.

[64] W. Liu, Z. Li, H. Cheng, C. Tang, J. Li, S. Zhang, S. Chen, J. Tian, *Adv. Mater.* **2018**, *30*, 1706368.

[65] F. Aieta, P. Genevet, M. A. Kats, N. Yu, R. Blanchard, Z. Gaburro, F. Capasso, *Nano Lett.* **2012**, *12*, 4932.

[66] A. Arbabi, E. Arbabi, S. M. Kamali, Y. Horie, S. Han, A. Faraon, *Nat. Commun.* **2016**, *7*, 13682.

[67] E. Maguid, I. Yulevich, M. Yannai, V. Kleiner, M. L. Brongersma, E. Hasman, *Light: Sci. Appl.* **2017**, *6*, e17027.

[68] B. E. A. Saleh, M. C. Teich, *Fundamentals of Photonics*, Wiley, Hoboken, NJ, USA **1991**.

[69] B. Xie, H. Liu, H. Cheng, Z. Liu, S. Chen, J. Tian, *Phys. Rev. Lett.* **2019**, *122*, 104302.

[70] E. D. Palik, *Handbook of Optical Constants of Solids*, Academic Press, New York, USA **1998**.